Acta Astronautica 245 (2026) 202–211

Contents lists available at ScienceDirect

Acta Astronautica

journal homepage: www.elsevier.com/locate/actaastro

Advancing CubeSat Thermal Management: In-orbit demonstration of a new heat sink technology☆,☆☆

Laryssa Sueza Raffa [a,*], Matt Ryall [b], Mohammad Arqam [a], Lee M. Clemon [c], Nick S. Bennett [a]

[a] School of Mechanical and Mechatronic Engineering, University of Technology Sydney, Ultimo, NSW 2007, Australia
[b] Mawson Rovers, Eveleigh, NSW 2015, Australia
[c] Mechanical Science and Engineering, The Grainger College of Engineering, University of Illinois Urbana-Champaign, Urbana, IL 61801, USA

ABSTRACT

With the rapid expansion of small satellite constellations in Low Earth Orbit (LEO), the demand for resilient computing and high-power electronics in telecom, surveillance, and scientific applications is rising. With increasing power densities, these systems face critical thermal challenges due to the absence of convective cooling and limited surface area for heat dissipation. Effective thermal management solutions are crucial for preventing overheating and ensuring mission longevity. This study presents a rare in-orbit performance assessment of an additively-manufactured triply periodic minimal surface (TPMS) heat sink with phase change material (PCM) for CubeSat thermal control. The University of Technology Sydney and Mawson Rovers' payload Matilda, launched aboard Waratah Seed-1 satellite in August 2024, integrates a thermal management module comprised of a 3D-printed aluminium TPMS structure with paraffin wax PCM, leveraging both the TPMS's high surface-area-to-volume ratio for enhanced heat transfer and the PCM's latent heat storage capacity. To establish a performance baseline, the payload also includes a conventional heat sink with radial planar fins without PCM, representative of widely-used terrestrial cooling solutions, and fabricated with identical metallic mass to the IWP TPMS heat sink. A comprehensive experimental analysis compares the in-orbit thermal behaviour of both modules, while a reduced-order numerical model enables rapid predictions of thermal performance with low computational effort. Results demonstrate that the TPMS-PCM-based module increased the time required for the electronics to reach an 85 °C setpoint temperature by 77% relative to the finned reference module. This substantial operating time extension was reached with an additional 7.0 g of PCM, which corresponds to only 16% mass increase relative to the mass of the metallic heat sinks, highlighting the effective performance of the TPMS-PCM-based thermal management module as a lightweight, high-impact solution. In addition, the reduced-order numerical model reproduced the overall transient orbital response with good agreement. These findings validate TPMS-PCM heat sinks as a scalable, lightweight thermal management solution for CubeSats, offering a pathway to extended operating time and enhanced reliability in next-generation small satellite missions.

1. Introduction

The growing use of CubeSats has amplified the need for reliable thermal control systems that can operate under harsh orbital conditions. These spacecraft are constrained by compact volumes, tightly packed high-power electronics, and limited surface area for heat rejection, making thermal management critical for mission success. Even minor temperature increases can accelerate component degradation, while modest reductions in operating temperatures significantly enhance reliability [1,2].

Passive thermal management solutions are particularly attractive for resource-limited space platforms, as they require no additional power or moving parts. Conventional finned heat sinks are widely used in terrestrial environments where convection dominates, but their effectiveness diminishes in space, where heat rejection is primarily via radiation. Integrating phase change materials (PCMs) into heat sink structures has gained attention, as PCMs offer high thermal storage per unit mass, buffering orbital temperature fluctuations, and extending electronics safe operating time [3,4].

Although PCMs were introduced for spacecraft thermal management several decades ago [5], experimental research under representative conditions remains scarce. Terrestrial studies have largely focused on improving PCM thermal conductivity through geometry optimisation, metal foams, or additively manufactured structures such as triply periodic minimal surfaces (TPMS) [6–9]. However, in-orbit demonstrations are rare and the performance of TPMS-PCM thermal management modules under orbital cycling remains poorly understood.

Numerical modelling offers a valuable tool for analysing PCM–heat sink behaviour, however full multi-physics simulations are often impractical for early design due to their high computational

☆ This article is part of a Special issue entitled: '76th IAC_invited only' published in Acta Astronautica.

☆☆ A preliminary version of this research was presented as paper IAC-25-B4-6B-10-x97595 at the 76th International Astronautical Congress (IAC), Sydney, Australia, 29 September - 3 October 2025.

* Corresponding author.
E-mail address: laryssa.suezaraffa@uts.edu.au (L. Sueza Raffa).

https://doi.org/10.1016/j.actaastro.2026.02.049
Received 5 December 2025; Received in revised form 23 January 2026; Accepted 25 February 2026
Available online 26 February 2026

Nomenclature

T	Temperature (°C unless specified otherwise)
t	Time (s)
P_{heater}	Heater power (W)
P_{module}	Power input on heat sink base surface (W)
P_{loss}	Power losses through satellite structure(W)
$\Delta\dot{E}_{module,stored}$	Change of thermal energy stored by the per unit time (W)
$\Delta\dot{E}_{heatsink,stored}$	Change of thermal energy stored by the heat sink per unit time (W)
$\Delta\dot{E}_{PCM,stored}$	Change of thermal energy stored by the PCM per unit time (W)
$q_{module,rad}$	Power dissipated via radiation (W)
Q	Thermal energy (J)
m	Mass (kg)
k	Thermal conductivity (W/mK)
C_p	Specific heat capacity (J/kgK)
H_{lat}	Latent heat capacity (J/kg)
A	Surface area (m^2)
V	Volume (m^3)

Subscripts

eff	Effective
sens	Sensible
lat	Latent
base	Heat sink's base surface
top	Heat sink's top surface
module	Module
structure	WS-1's internal structure
∞	Surroundings
metal	Metal of heat sink
air	Air inside the heat sink
PCM	PCM
HS	heat sink
l	Liquidus
s	Solidus
shift	Time phase shift

Greek symbols

ρ	Density (kg/m^3)
λ	Liquid fraction of PCM (dimensionless)
σ	Stefan–Boltzmann constant (5.67×10^{-8} W · $m^{-2} \cdot K^{-4}$)
ϵ	Emissivity

Acronyms/Abbreviations

IWP	I-graph-wrapped package
LPBF	Laser powder bed fusion
LEO	Low Earth Orbit
PCM	Phase Change Material
TPMS	Triply Periodic Minimal Surface
TVAC	Thermal Vacuum Chamber
WS-1	Waratah Seed-1 CubeSat

effort. Reduced-order models that represent the PCM–metal pair as a homogeneous solid with effective thermophysical properties offer an efficient alternative, capturing overall thermal behaviour while reducing computational time and demand [10–13].

This work addresses the critical gap in experimental data by presenting rare in-orbit performance results of a novel thermal management module comprised of an additively manufactured TPMS heat sink integrated with paraffin wax PCM, flown within the University of Technology Sydney and Mawson Rovers' payload Matilda aboard the Waratah Seed-1 CubeSat. Integrating also a conventional heat sink of planar fins used as a baseline, Matilda enables direct comparison between both thermal management modules, with particular focus on thermal improvements imposed by the PCM and the TPMS-enhanced internal structure under cyclic solar–eclipse conditions. In addition, a reduced-order numerical model, calibrated against flight data, is developed to enable a computationally efficient framework for early-stage thermal design.

2. Payload

Together, the University of Technology Sydney and Mawson Rovers have developed Matilda, a payload to demonstrate a passive thermal management concept in orbit, with particular focus on evaluating the performance of an additively manufactured TPMS-PCM temperature regulation module under real spaceflight conditions. Matilda was housed within the Waratah Seed-1 CubeSat, a 6U platform providing shared access to Australian payloads, launched in August 2024 on the Transporter-11 mission aboard a SpaceX Falcon 9.

The Waratah Seed-1 CubeSat, managed by the ARC Training Centre for CubeSats, UAVs, and Their Applications (CUAVA), is Australia's first rideshare CubeSat envisioned to enable affordable orbital access for local research groups, universities, and start-ups [14]. Nine payloads, including Matilda, were flown on this mission to demonstrate emerging technologies in the space environment.

2.1. CubeSat integration

The payload is located inside the WS-1 structure, which is built from aluminium alloy with a thickness of roughly 2 mm. The structure is enclosed with solar panels, GPS and S-band antennas, and an Earth sensor [14]. This enclosure provides structural integrity while shielding internal systems from direct solar flux, Earth albedo, and infrared radiation. Within the satellite interior, thermal coupling occurs primarily through conduction across structural interfaces and radiation heat exchange with neighbouring subsystems such as the power units, avionics boards, and battery packs [14].

2.2. Payload architecture

The Matilda payload consists of two thermally independent units mounted in a stacked configuration, as illustrated in Fig. 1(b). Each unit integrates a dedicated printed circuit board (PCB) with a resistive plane heater and multiple thermistors. A metallic heat sink is bonded to the heater to provide passive dissipation of the generated heat. The upper unit functions as the baseline reference case, incorporating a traditional heat sink with internal planar radial fins not containing PCM, commonly used on Earth for cooling electronics. The lower unit implements the experimental concept: a TPMS I-graph-wrapped package (IWP) lattice structure loaded with 7.0 g of PCM.

2.2.1. Heat sinks

Both heat sinks were produced in aluminium alloy F357 (Al-Si7-Mg) via laser powder bed fusion (LPBF) from a GE Concept Laser M2 Series 5 machine equipped with a 400 W laser. After LPBF fabrication, the heat sinks underwent thermal treatment to reduce residual stress and ultrasonic cleaning to remove trapped powder. External contact surfaces were then machined to ensure adequate flatness and surface quality for temperature sensing. The main properties of the stress-relieved material are summarised in Table 1 [15]. Additive manufacturing was chosen for its ability to fabricate complex geometries

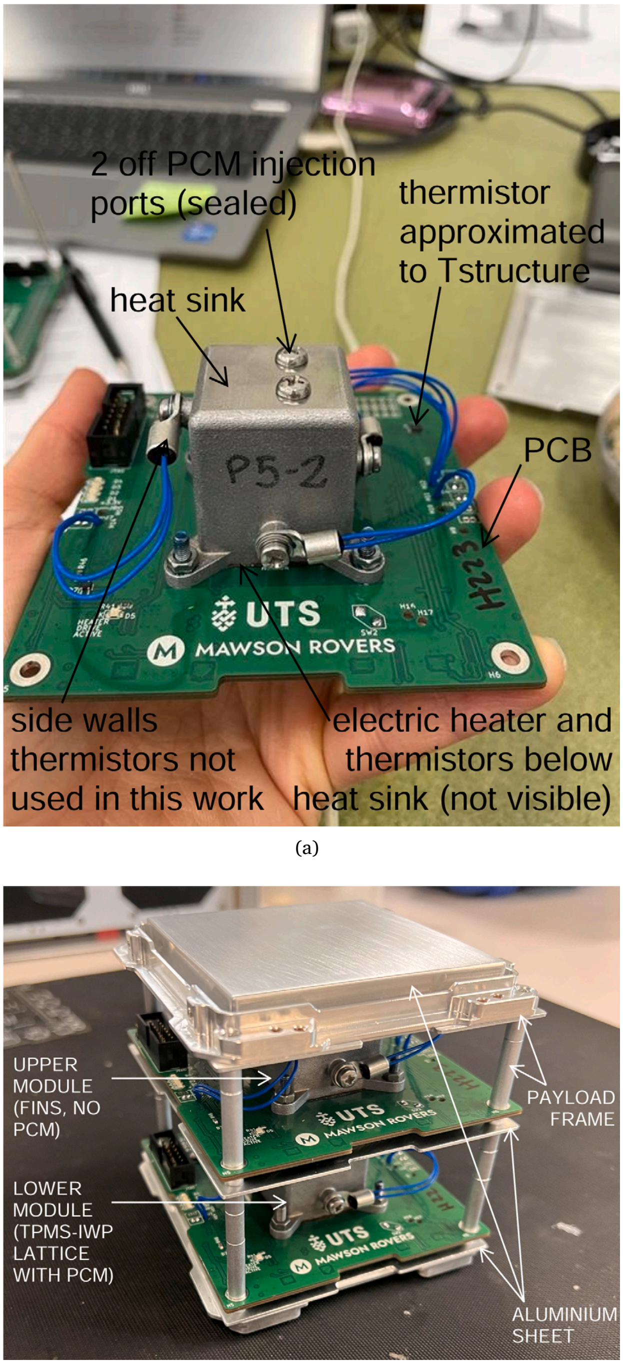

(a)

(b)

Fig. 1. (a) Picture of one of the thermal management modules of the Matilda payload. (b) Picture of Matilda payload (note that the PCM injection ports of the top surface of both heat sinks are present in the payload, although unable to be visualised due to angle of picture).

such as the IWP lattice used in the TPMS design, the rapid turnaround required to meet the tight payload development schedule, and the capacity to produce the heat sink as a single component, minimising interfaces and reducing the chances for PCM leakage during phase change expansion.

The radial-finned heat sink was selected as a benchmark due to its widespread use in terrestrial electronics cooling, providing a conventional reference for comparison. The IWP lattice geometry was selected based on the authors' previous design-comparison study in vacuum, where it exhibited strong mass-normalised thermal performance and reduced sensitivity to orientation relative to fin-based PCM heat sinks, demonstrating strong potential for reduced-gravity applications [16]. The two heat sink designs, presented in Fig. 2, were manufactured with matching outer dimensions: 30 mm × 30 mm base, 34 mm height, 2 mm thick sidewalls, and a 3 mm thick top plate. Refer to Appendix B for more details. Their metallic masses are also nearly identical, at 42.3 g for the finned version and 43.4 g for the lattice version, ensuring a fair evaluation of thermal behaviour without geometric or mass biases [16]. The reference heat sink employs a radial fin array and contains no PCM, as conventionally used in electronics cooling terrestrially. The enhanced design features an IWP lattice with 7 mm cells within the heat sink and was filled with 7.0 g of organic PCM (paraffin wax Sigma-Aldrich 327204, material properties listed in Table 1).

The chosen PCM mass of 7.0 g for the IWP TPMS module corresponds to roughly 60% of the heat sink internal cavity volume in the solid state, intentionally leaving sufficient void space to accommodate PCM volumetric expansion during melting. This design consideration is particularly important under vacuum operation, where paraffin exhibits larger volume change during melting [12], increasing the risk of leakage due to the high ratio between internal and external pressure. The adopted filling fraction was established empirically prior to flight through incremental PCM filling and subsequent vacuum operation until leakage was first observed, defining a conservative upper limit. Estimates based on internal and external pressure differentials from the literature [17] indicated a comparable allowable filling volume. In preparation of the payload, the PCM filling process was carried out by heating the IWP-TPMS heat sink above the PCM melting point and injecting liquid paraffin through dedicated ports on the top surface (Fig. 1(b)). Maintaining the heat sink above the melting range ensured continuous PCM flow and promoted uniform distribution within the internal cavity. After injection, the ports were prepared and closed with appropriate gaskets and fasteners while the PCM was still molten (expanded), thereby limiting trapped air and reducing the risk of pressure build-up during subsequent operation. The module was fully cooled naturally to room temperature prior to final assembly. PCM leak checks were performed prior to launch through multiple thermal cycles under medium-grade vacuum conditions, with no leakage observed based on visual checks, mass consistency, and repeatable temperature responses across cycles. Note that once the payload was integrated onto WS-1, high-grade vacuum testing was conducted in the Wombat-XL vacuum chamber as part of the mission's pre-flight environmental testing campaign. Although post-test mass comparison was not possible due to permanent integration of the payload into WS-1, residual gas analyser measurements performed within the Wombat-XL TVAC after the thermal-vacuum cycling indicated no detectable outgassing attributable to the PCM.

The payload was assembled as follows. A thin film of thermal grease (reference Apiezon H) was deposited at the heater–sink contact to reduce thermal resistance, after which each sink was mechanically fastened to the PCB via bolted connections (Fig. 1(b)). Both units were later arranged in a vertical stack within a 1U frame, positioning the TPMS-PCM unit on the lower part and the finned reference unit on the upper part (Fig. 1(b)). To minimise heat transfer between the units and between adjacent payloads, aluminium sheets were placed under the bottom unit, amid both units, and above the upper unit.

2.2.2. Heater and temperature sensing

The planar resistive heater embedded in each unit's PCB provided a controlled heat flux over a 30 × 30 mm area to simulate the waste heat generated by onboard electronics in small satellites. The system operated from the satellite's 5 V power bus, with the average potential across the heater terminals recorded as 4.9 V by the payload's internal electronics. The electrical resistance of the heater was experimentally determined in relation to the electronics temperature (T), yielding a

Table 1
Material properties [15,18,19].

Property	Aluminium	PCM
	(Al-Si7-Mg)	(Sigma-Aldrich 327204)
ρ (kg/m^3)	2670	880
k (W/mK)	150	0.2
Melting point (°C)	–	53–58
C_p (J/kgK)	960	2000
H (J/kg)	–170 000	

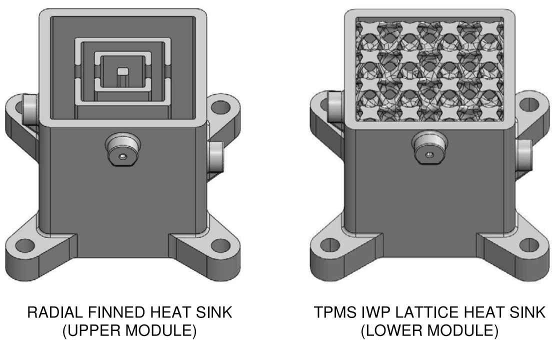

Fig. 2. Designs of the two heat sinks integrated in the Matilda payload (top surface hidden for better visualisation of internal structure).

linear correlation. With the voltage and resistance, the instantaneous electrical power delivered to the heater, P_{heater} was then determined by Ohm's law as shown in Eq. (1). The heater supplied between 7.2–7.8 W at the start of each run, depending on the initial electronics temperature. Due to heat losses through the payload structure, empirically determined in Appendix A, the actual heat flux acting on the base surface of the thermal management module, P_{module}, is given by Eq. (2). The uncertainty in power was estimated at ± 0.21 W, following the error propagation of voltage and resistance measurements described in previous work [20].

$$P_{heater} = \frac{4.9^2}{0.0192T + 2.7774} \tag{1}$$

$$P_{module} = P_{heater}(-0.002127(T - T_{structure}) + 1.005222) \tag{2}$$

Temperature monitoring was achieved with five thermistors (Vishay NTCS0603E3103FMT) integrated into the heater PCB. The central sensor consistently registered the maximum temperature and was thus adopted to represent the electronics temperature, being referenced to as "electronics temperature" T throughout. A sixth thermistor was embedded in the PCB near the southeast payload mounting standoff, as indicated in Fig. 1(a). This thermistor was approximated to the satellite's internal structure temperature referred to as $T_{structure}$, as detailed in Section 3.1.3. Data were sampled at 5-second intervals.

3. In-orbit experimental works

WS-1 operates in a near-polar orbit with an inclination of 97.43°, a low eccentricity of 0.00039, and an altitude ranging between roughly 500 and 520 km [21]. For the orbit analysed on 2nd November 2024 (UTC) WS-1 operated at a solar beta angle of about 17°. Under these orbital conditions, the satellite completes around 15 revolutions per day, with each orbit lasting approximately 94.7 min. From this orbital cycle duration, roughly 35 min are spent in eclipse and about 60 min in solar illumination. As illustrated in Fig. 3, four representative orbital positions are used as a reference throughout this work:

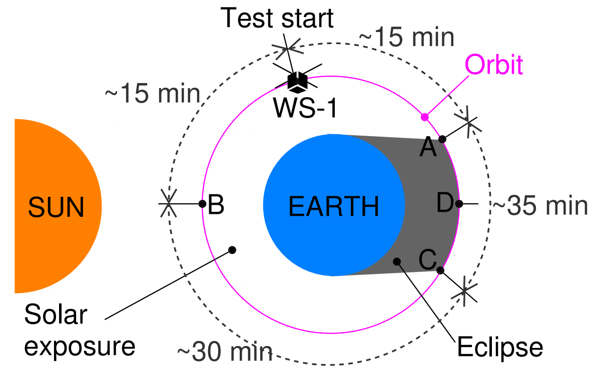

Fig. 3. Orbital schematic of the WS-1 satellite (not to scale), highlighting positions A–D: eclipse exit, maximum solar exposure, eclipse entry, and mid-umbra, respectively.

- Position A: eclipse exit, when the spacecraft transitions into sunlight.
- Position B: peak solar exposure, corresponding to maximum insolation.
- Position C: eclipse entry, marking the onset of shadowing in eclipse.
- Position D: mid-eclipse, where the satellite is at the core of the eclipse.

To quantify the natural electronics temperature variations, including their maximum and minimum values, idle runs (with heaters switched off) were conducted over 14 orbital cycles. Subsequently, controlled heating–cooling experiments were performed for each module. These experiments were initiated approximately 15 min after eclipse exit, providing about 45 min of solar exposure from the experiment start, as illustrated in Fig. 3. Heating continued up to 85 °C, at which point the heater was turned off and the cooling response was recorded. The selected temperature limit corresponds to the upper operational range commonly reported for CubeSat electronic hardware in the literature [22]. To maintain consistent initial conditions, each module was tested one orbit apart, ensuring comparable starting temperatures. These heating–cooling results are discussed and are subsequently used to validate the numerical model developed in Section 3.1. Note that due to the operational constraints of the Waratah Seed-1 rideshare mission [14], only a single in-orbit heating–cooling cycle was executed for each thermal management module. As a result, potential changes in PCM behaviour across several orbital cycles could not be directly evaluated within this campaign. However, organic PCMs are known to present long-term stability of across several thermal cycles. As an example, Katish et al. [23] conducted 10,000 phase change cycles on paraffin waxes and reported that all materials kept their initial properties, including latent heat capacity and melting behaviour, which was also confirmed through spectroscopic analyses which pointed to no significant molecular changes.

3.1. Reduced-order numerical simulation

A reduced-order numerical model was employed to predict the behaviour of the thermal management modules. The model treats each module as a homogeneous solid with lumped mass and effective thermophysical properties, namely thermal conductivity k_{eff}, specific heat capacity $C_{p,eff}$, and density ρ_{eff}. Comparable simplified modelling strategies have been reported in the literature to minimise computational cost [10,11]. The effective properties are detailed in the following sections and summarised in Table 2.

3.1.1. Effective thermal conductivity

The effective thermal conductivity of the homogeneous solid, k_{eff}, was estimated using a series–parallel formulation (Equation (3)) [24, 25]. Note that this estimation approach was previously validated against experimental measurements in the authors' previous work [20]. The terms in Eq. (3) capture the weighted contributions of the metallic structure, the internal air void left to accommodate PCM expansion during melting, and the PCM itself, as applicable for each module of the payload. The overall external volume of the heat sink is given by the sum of V_{metal}, V_{air}, and V_{PCM}.

$$k_{eff} = \frac{k_{metal}V_{metal} + k_{air}V_{air} + k_{PCM}V_{PCM}}{V_{total}} \tag{3}$$

While the heat sinks, especially the finned design, could exhibit some anisotropic thermal behaviour, for the purposes of this reduced-order approach the heat sinks were idealised as homogeneous, isotropic bodies. This simplification was adopted to prioritise computational efficiency while retaining predictive accuracy, an assumption commonly applied in spacecraft thermal modelling [10,11]. Validation presented in authors' earlier works [12,20] demonstrated that this approach remains reliable within the scope of this study.

3.1.2. Effective specific heat capacity

For the heat sink without PCM, the effective specific heat capacity $C_{p,eff}$ was taken as the value of the metallic material alone. In the case of the PCM-filled heat sink, the latent heat of paraffin was incorporated as an enlarged specific heat capacity within its melting interval, consistent with prior approaches reported in the literature [26–28]. As a result, the composite material exhibits three regimes of $C_{p,eff}$: below the melting range, within the melting range, and above it. Outside the phase transition interval, $C_{p,eff}$ was evaluated through a volume-weighted mixture of the metal and paraffin contributions. Within the melting range (T_l – T_s), the total latent heat of the paraffin was included as an additional energy-storage term, yielding the formulation in Eqs. (4)–(5). This representation allows the latent heat effect to be captured using an equivalent specific heat capacity, avoiding the need for multi-phase, multi-physics modelling and thereby reducing computational requirements.

$$Q_{eff} = Q_{HS,sens} + Q_{PCM,sens} + Q_{PCM,lat} \tag{4}$$

$$m_{eff}C_{p,eff}(T_l - T_s) = m_{HS}C_{p,HS}(T_l - T_s) + m_{PCM}C_{p_{PCM}}(T_l - T_s) + m_{PCM}H_{lat,PCM} \tag{5}$$

It is assumed that the PCM and the metallic structure are at thermal equilibrium and that the entire PCM mass undergoes phase change between T_l and T_s. Solving Equation (5) for $C_{p,eff}$ yields the effective specific heat capacity of the composite within the PCM melting interval.

3.1.3. Numerical simulations

Finite element simulations were carried out using ANSYS Fluent 2021. A 3D body with a cuboid geometry of 30 x 30 mm base and 34 mm height was created to represent each module. Given the simplicity of the geometry, a hexahedral mesh with uniform elements sized 0.5 mm was employed. A custom material was defined in Ansys Fluent to represent the effective composite properties k_{eff}, $C_{p,eff}$, and ρ_{eff}, listed in Table 2. The effective density was obtained through a volume-weighted mixture of the metallic heat sink and paraffin PCM contributions.

Because the reduced-order approach concentrated on conduction within a homogeneous solid body, the flow equation was disabled, leaving just the energy equation to be solved. The governing relation for transient heat conduction in a solid is expressed as follows:

$$\rho_{eff}C_{p,eff}\frac{\partial T}{\partial t} = k_{eff}\left(\frac{\partial^2 T}{\partial x^2} + \frac{\partial^2 T}{\partial y^2} + \frac{\partial^2 T}{\partial z^2}\right) \tag{6}$$

For boundary conditions, a radiation-only model was considered, with side walls and top surface of the composite body rejecting heat to ambient. The ambient temperature was approximated by the internal structural temperature of WS-1, $T_{structure}$, approximated to the thermistor on the PCB of the finned module adjacent to the mounting standoff, as detailed in Sections 2.2.2 and 4.1. $T_{structure}$ was inputted into the simulations as a time-dependent user-defined expression given by Eq. (8). The heat flux acting at the bottom surface of the sink was also inputted as a temperature-dependent user-defined expression from Eq. (2).

Table 2
Effective thermo-physical properties of the composite, homogeneous solids created for each module for the reduced-order numerical simulation.

Property	Fins, no PCM	IWP-TPMS, PCM
ρ_{eff} (kg/m^3)	1235	1641
k_{eff} (W/mK)	78	71
$C_{p,eff}$ (J/kgK)	963	1107 (T < 53 °C) 1107 (T > 58 °C) 5820 (53–58 °C)

Boundary condition imposed at the heat sink external surface - Radiation:

$$-k_{eff}\frac{\partial T}{\partial n} = \epsilon\sigma A\left(T^4 - {T_{structure}}^4\right) \tag{7}$$

The initial and boundary conditions are summarised below:

1. Initial temperature of solid: extracted from the in-orbit experiments (specifically 8.5 °C for the reference heat sink with radial fins and no PCM, and 9.3 °C for the PCM-based IWP-TPMS heat sink).
2. Ambient temperature: adopted as WS-1 internal structural temperature $T_{structure}$, as outlined in Section 2.2.2.
3. Uniform heat flux imposed to the base surface, P_{module}, determined from Eq. (2).
4. External walls and upper surface: heat transfer through radiation only, with an adopted emissivity of 0.25 [29].

4. Results and discussion

The results of this work are presented in two stages to build an understanding of the thermal performance of the two modules in orbit. The in-orbit experimental results are introduced, beginning with the idle orbital cycles to characterise the internal spacecraft thermal environment and followed by the active heating and cooling experiments of both modules. Finally, these datasets are used to validate the reduced-order numerical model developed for both the finned and TPMS-PCM-enhanced heat sinks. This structure ensures a logical progression from experimental quantification of heat inputs, through in-orbit performance assessment, to the verification of the numerical modelling framework.

4.1. In-orbit experimental results

As outlined in Section 2.2.2, the internal structural temperature of the satellite was approximated using data from the thermistor located on the finned module's PCB near the southwest standoff for simplicity at this stage. Fig. 4 reports the thermistor's temperatures, denoted $T_{structure}$ throughout, for a total of 14 idle cycles (no heating). As expected from the orbital day–night cycles, $T_{structure}$ varies periodically, peaking near full solar illumination (Fig. 3, position B) and reaching a minimum in eclipse (position D). This trend aligns with numerical spacecraft thermal simulations reported in the literature [22,30], where internal structural temperatures are shown to vary in phase with orbital illumination conditions. The maximum and minimum internal structural temperatures, $T_{structure}$, are summarised in Table 3. A cosine curve was fitted to the idle data and will be used as an input for the numerical model in Section 4.2. Using the average valley and peak temperatures

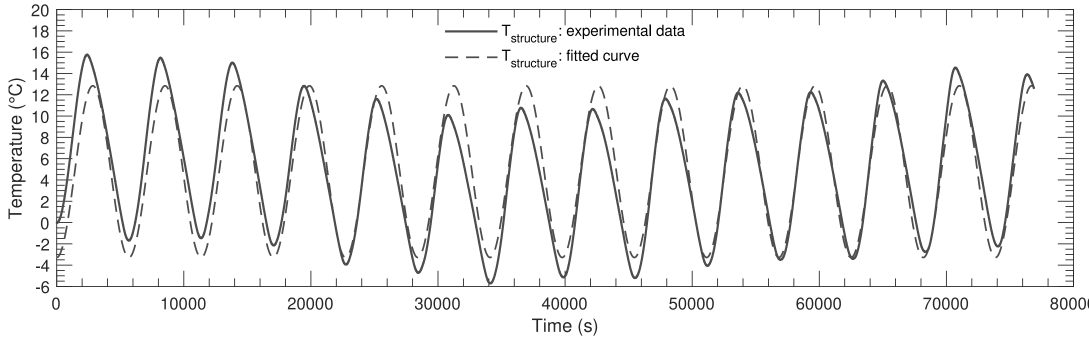

Fig. 4. In-orbit experimental results: transient $T_{structure}$ for 14 idle orbits (no heating), initiated at UTC 02/11/2024 3:00:41 PM. Fitted curve as per Equation (8) also displayed.

Table 3
Minimum and maximum $T_{structure}$ recorded in idle orbital cycles (no heating), obtained from Fig. 4.

Cycle No.	Minimum (°C)	Maximum (°C)
Cycle 1	0	15.7
Cycle 2	−1.7	15.4
Cycle 3	−1.4	15.0
Cycle 4	−2.1	12.8
Cycle 5	−3.9	11.6
Cycle 6	−4.7	10.1
Cycle 7	−5.6	10.8
Cycle 8	−5.1	10.7
Cycle 9	−5.2	11.6
Cycle 10	−4.1	12.2
Cycle 11	−3.5	12.2
Cycle 12	−3.4	13.3
Cycle 13	−2.7	14.5
Cycle 14	−2.2	13.9
Average	−3.3	12.8

of Table 3, the mean temperature was calculated at 4.8 °C, and the amplitude of the cosine curve was calculated at 8.1 °C. With the orbital period (94.7 min = 5682 s), the cosine representation of the internal structural temperature $T_{structure}$ is:

$$T_{structure}(t) = 4.8 - 8.1cos\left(\frac{2\pi}{5682}[t + t_{shift}]\right) (°C) \quad (8)$$

where t is the elapsed time in seconds, and t_{shift} is the phase shift that aligns the cosine with the start of the dataset (set to 0 s in Fig. 4). Thermal inertia between solar position and internal temperature are neglected for simplification.

Fig. 5 then presents the active heating and cooling responses of both modules. As described in Section 3, each heating sequence was initiated in sunlight, approximately midway between the eclipse exit and maximum solar exposure (positions A and B of Fig. 3). The internal structural temperature of WS-1, $T_{structure}$, is also shown for reference. At the start of the heating phases, the electronics next to the finned heat sink without PCM were at 8.5 °C. For the IWP-TPMS PCM case, the initial temperature was slightly higher at 9.3 °C. Representing a reference design often used to thermally regulate electronics on Earth, the heat sink with fins achieved the 85 °C setpoint temperature after approximately 660 s. The IWP-TPMS PCM module, in turn, extended this time to roughly 1165 s. Stemming from the combined effect of PCM's latent heat absorption and increased internal surface area and improved geometry distribution to promote heat transfer from metal to PCM, this significant extension in operating time of 77% was obtaining with an increase in mass of only 7.0 g (referent to the PCM). Accounting for measurement and sampling uncertainties as established in authors previous work [20], the reported increase in operating time carries an estimated uncertainty of about ±2%. To contextualise these findings, a previous in-orbit study by the authors [31] under different orbital position also reported a significant improvement imposed by the TPMS-PCM pair. In that case, heating began with the reference finned heat sink exiting solar exposure and entering penumbra, and with the IWP TPMS-PCM module in penumbra. Under those conditions, the TPMS-PCM extended the time to reach 85 °C by approximately 92% relative to the finned baseline, highlighting its sensitivity to orbital thermal boundary conditions, particularly the timing of solar exposure.

Although this work primarily focuses on in-orbit performance, a qualitative comparison with terrestrial high-grade vacuum testing is provided for context. The terrestrial data was used as the results from the experiments conducted in the Wombat-XL TVAC (Fig. A.1) to determine the heat losses from the heater input in Appendix A. Note, however, that these terrestrial experiments were conducted under low ambient temperatures (approximately -27 °C), whereas the in-orbit experiments were initiated during solar exposure (Fig. 5), corresponding to different boundary conditions. Under terrestrial high-grade vacuum, the time required to achieve 85 °C went from approximately 680 s for the finned module to 1260 s for the case of IWP TPMS-PCM, corresponding to an extension in operating time of about 85%. Despite the differing ambient environments and boundary conditions, the relative performance improvement provided by the PCM-enhanced IWP TPMS design was comparable across both cases. A detailed comparative analysis between terrestrial high-grade vacuum and orbital operation with a corresponding thermal boundary condition is outside the scope of the present study and is addressed by the authors in a separate study [31].

4.2. Reduced-order numerical modelling

To enable thermal predictions requiring low computational demand, the developed reduced-order numerical modelling used effective thermo-physical properties for a composite, uniform solid for each thermal management module with these effective properties listed in Table 2. The numerical model was validated against the in-orbit results presented in Fig. 5, as follows.

Figs. 6(a) and 6(b) present the validation of the reduced-order numerical modelling for the finned heat sink without paraffin, and the IWP-TPMS PCM heat sink, respectively, referent to the orbital results presented in Fig. 5. A good agreement was observed between the model and the experimental data for both thermal management modules. For the module with fins and no PCM, the model diverges from the experimental results by providing a faster temperature rise rate throughout the heating process, observed by the slope of the temperature curve. The largest discrepancy between experimental data and simulation results was observed at 4.0 °C, around 25 s into heating.

For the IWP-TPMS module with PCM, the simplified model generally provided lower temperatures than those measured in orbit, particularly during the pre-melting phase and throughout the phase change of the PCM. The numerical model reproduces the plateauing behaviour imposed between 53 °C and 58 °C, corresponding to the specified range

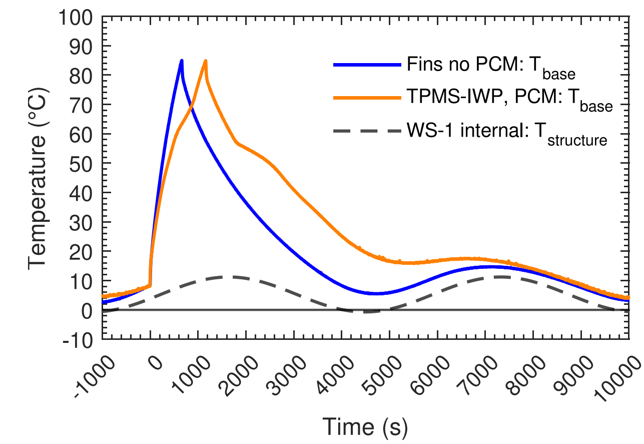

Fig. 5. In-orbit heating (100% duty cycle) and cooling response of both modules to 85 °C setpoint. Temperature measurements for the finned module without PCM was initiated at UTC 26/11/2024 3:29:36 AM and the recordings for the TPMS-PCM module started at UTC 26/11/2024 5:04:39 AM. Fitted internal structure temperature (Equation (8)) shown for reference.

in which $C_{p,eff}$ was increased to account for the PCM's latent heat absorption. In contrast, the experimental results indicated a broader and higher melting interval, with T_{base} plateauing from approximately 58 °C to 68 °C. This suggests that, in practice, longer time may be required for heat to conduct from the metallic heat sink base into the TPMS lattice and then into the PCM, such that, when PCM finally begins melting, the base of the heat sink is at a higher temperature than the actual PCM. This effect cannot be captured by the homogeneous composite assumption used in the model. The largest discrepancy, about 6.6 °C, occurred near 750 s during the PCM melting process. Since most of the observed differences were observed before and during PCM melting, they may be related to the melting dynamics and internal redistribution of PCM under microgravity, as well as possible interactions with residual trapped air inside the heat sink cavity. PCM behaviour under microgravity remains insufficiently characterised in the literature and, in future works, detailed numerical model that includes PCM volumetric expansion, its viscosity, and its interaction with trapper air under microgravity should be developed to provide clarity. However, it was also noted that the finned module without PCM showed deviations from the orbital data, implying that part of the discrepancy may originate from the approximation of the internal satellite structure temperature, $T_{structure}$, as the thermostat located in the payload PCB near the standoffs. This approximation may not fully represent the actual structural temperature of WS-1, possibly due to not modelled radiative heat exchange with adjacent payloads whose thermal states were not monitored, as is typical in rideshare missions.

Overall, despite deviations of up to 6.6 °C for the IWP-TPMS module with PCM, the reduced-order model sufficiently reproduced the transient thermal behaviour of both finned and PCM-enhanced modules under orbital conditions, with low computational demand. These results validate the model's suitability as a quick and low effort predictive tool for preliminary design studies PCM-based thermal management modules for space applications.

5. Conclusions

This study presented the orbital thermal performance of two passive thermal management modules within the University of Technology Sydney and Mawson Rovers' Matilda payload: a conventional radial plane fins heat sink without PCM and a IWP TPMS heat sink with PCM. Both heat sinks were fabricated from aluminium and featured identical external dimensions, wall thickness, and metal mass. The two designs differed only in their internal geometry and the inclusion of PCM, with the IWP-TPMS design incorporating 7.0 g of paraffin wax PCM. Experimental results demonstrated that PCM integrated into the IWP TPMS significantly extended the operational time before electronics reached the 85 °C threshold, by approximately 77% relative to the finned baseline, with only 16% extra mass attributable solely to the added PCM.

The reduced-order numerical model, based on equivalent thermophysical properties for homogeneous composite solids, was validated against the in-orbit dataset for both modules. Despite maximum deviations of up to 6.6 °C for the PCM-enhanced module during the melting phase, the model reproduced the overall transient temperature behaviour with good accuracy across power levels and environmental conditions. Its low computational demand confirms the suitability of the approach as a rapid predictive tool for preliminary design studies of PCM-based CubeSat thermal control systems. However, the simplifications in the reduced-order formulation, particularly the homogenisation of PCM behaviour, limit the model's ability to capture effects such as delayed PCM melting due to metal-to-PCM heat transfer, PCM dynamics in microgravity, PCM interactions with trapped air inside the heat sink's cavity, and the influence of surrounding spacecraft structures and payloads. As future works, a more detailed multiphysics simulation would be required to account for these effects and to model the full satellite environment. In addition, longer orbital missions would be beneficial to assess the long-term stability of PCM in orbit.

While the experimental demonstration presented in this study was performed on a specific CubeSat form factor and thermal load, the proposed TPMS-PCM thermal management concept can be scaled in

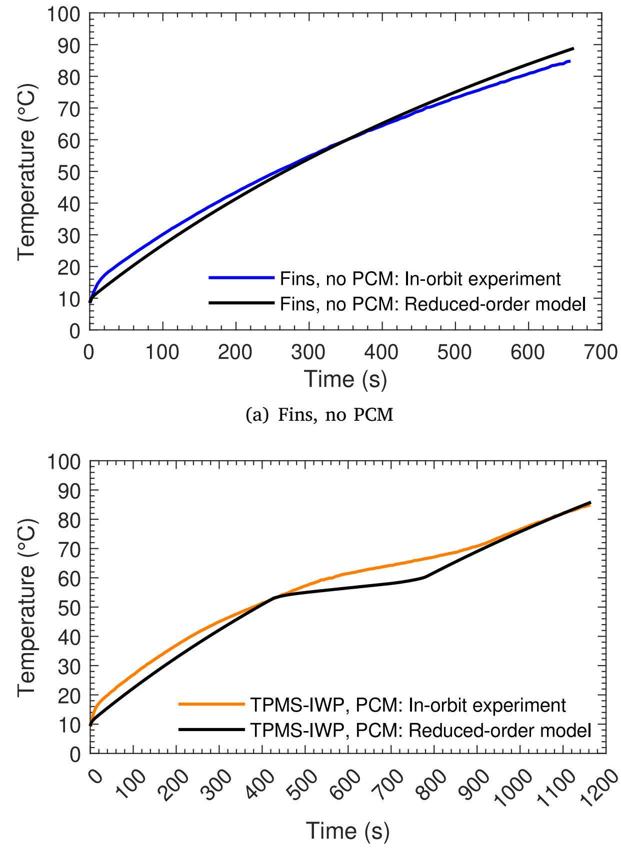

(a) Fins, no PCM

(b) IWP-TPMS, PCM

Fig. 6. Reduced-order numerical model validation against in-orbit demonstration: (a) Finned heat sink without PCM; (b) IWP lattice TPMS with PCM.

an architectural and methodological sense to other configurations. Key parameters of the TPMS lattice geometry, including unit cell size, porosity, overall envelope dimensions, and wall thickness, can be modified, while PCM material properties and mass may be selected to accommodate different heat dissipation requirements, allowable temperature limits, and volume constraints. In this context, the reduced-order numerical framework developed in this study provides a practical design tool, enabling rapid assessment of alternative configurations under varying thermal loads and constraints.

In conclusion, the University of Technology Sydney and Mawson Rovers' payload Matilda was successfully demonstrated in orbit, showcasing the effectiveness of the novel PCM-based IWP-TPMS thermal management module in delivering substantial thermal regulation and extending electronics operating time, enhancing electronics reliability. Complementing these results, the reduced-order numerical model proved to be a simple yet efficient tool for early-stage design, enabling quick assessment of passive PCM-integrated thermal management strategies for space applications.

CRediT authorship contribution statement

Laryssa Sueza Raffa: Writing – original draft, Validation, Methodology, Investigation, Formal analysis, Data curation. **Matt Ryall:** Software, Resources. **Mohammad Arqam:** Resources. **Lee M. Clemon:** Writing – review & editing, Supervision. **Nick S. Bennett:** Writing – review & editing, Supervision, Funding acquisition, Conceptualization.

Declaration of competing interest

The authors declare that they have no known competing financial interests or personal relationships that could have appeared to influence the work reported in this paper.

Acknowledgements

This research was funded by the University of Technology Sydney, Australia, SmartSat Cooperative Research Centre , Australia, and the Australian Government Research Training Program, Australia.

Appendix A. Determination of heat losses through the satellite structure and net heat flux applied at the heat sink's base

To determine heat losses through the satellite structure and, the actual heat flux applied at the base surface of the heat sink, preliminary ground-based heating runs were conducted in a controlled ambient, prior to flight. These terrestrial tests were performed in the Wombat-XL thermal vacuum chamber at the National Space Test Facility on

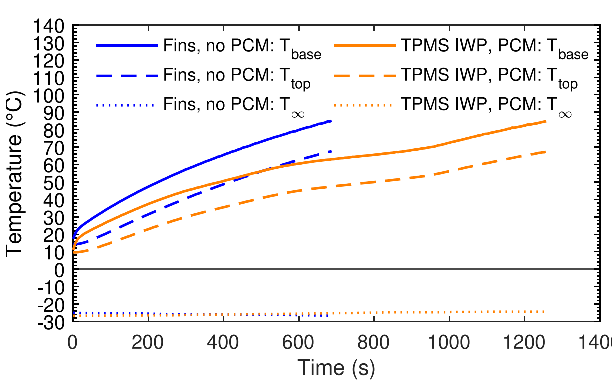

Fig. A.1. Experimental results for terrestrial tests in the Wombat-XL TVAC: T_{base} and T_{top} for both modules assembled onto WS-1 Cubesat (finned heat sink without PCM and TPMS IWP lattice heat sink with PCM).

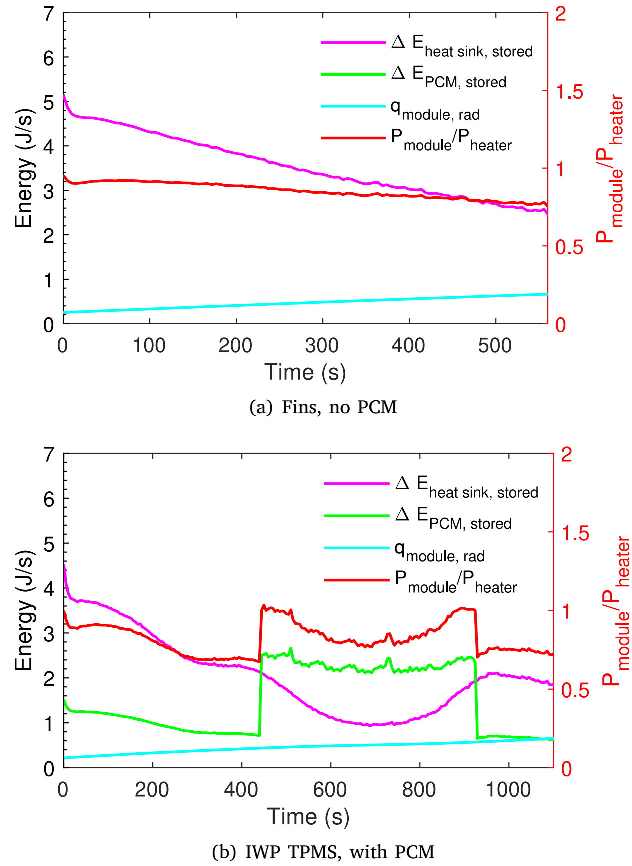

(a) Fins, no PCM

(b) IWP TPMS, with PCM

Fig. A.2. Transient energy components: $\Delta\dot{E}_{heatsink,stored}$, $\Delta\dot{E}_{PCM,stored}$, $q_{module,rad}$, and P_{module}/P_{heater} for both modules: (a) Finned heat sink, no PCM; and (b) IWP-TPMS heat sink with PCM.

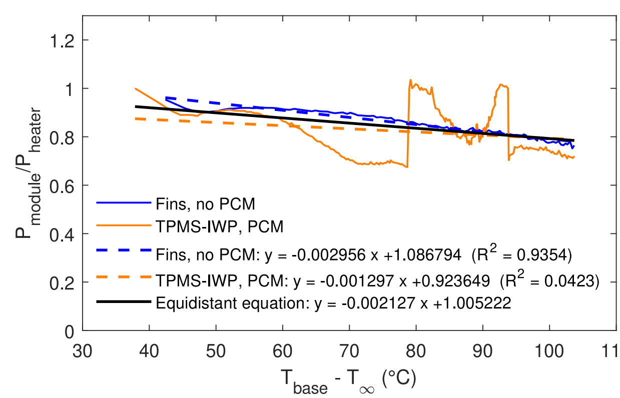

Fig. A.3. Empirical linear correlations for P_{module}/P_{heater} as a function of $T_{base} - T_{\infty}$ for both modules.

Canberra, Australia. Thermographic infrared images resulting from these test runs enabled visual observation that a fraction of the power released by the electric heater escaped through the satellite's structure, therefore not being fully applied at the base surface of the heat sink. This behaviour has also been reported in the authors' earlier work, based on an isolated experiment where a single heat sink was tested an assembly mount rather than within the payload integrated into the CubeSat [20]. The total heater power, P_{heater}, can be represented as the sum of the effective heat delivered to the base of the heat sink, P_{module}, and the parasitic losses through the mount, P_{loss}, as shown in Eq. (A.1).

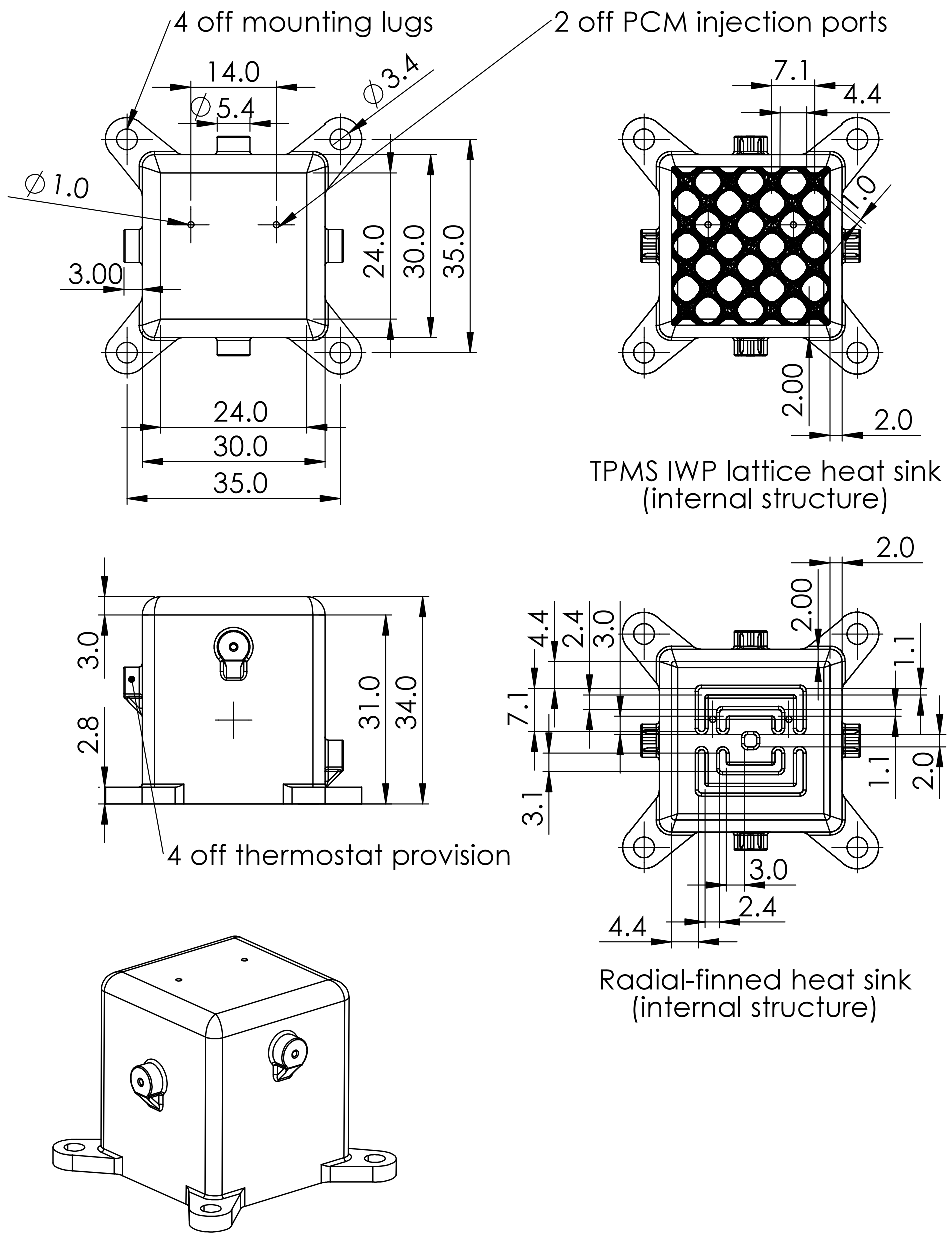

Fig. B.4. Drawings of the IWP-TPMS heat sink and the radial-finned heat sink used in this work. Note: both heat sinks present identical external dimensions and features; internal geometries as shown.

P_{module} is partly retained within the heat sink and PCM, and partly rejected to ambient at the heat sink's external surfaces. Hence, P_{module} was determined from a combination of stored and rejected energy terms, following the formulation in Eqs. (A.2), (A.3), and (A.4a).

This methodology is consistent with approaches reported in the literature [32].

$$P_{heater} = P_{module} + P_{loss} \quad (A.1)$$

$$P_{module} = \Delta\dot{E}_{module,stored} + q_{module,rad} \quad (A.2)$$

$$q_{module,rad} = \epsilon\sigma A(T^4_{module} - T^4_{\infty}) \quad (A.3)$$

$$\Delta\dot{E}_{\text{module, stored}} = \Delta\dot{E}_{\text{heat sink, stored}} + \Delta\dot{E}_{\text{PCM, stored}}, \quad (A.4a)$$

$$\Delta\dot{E}_{\text{heat sink, stored}} = \frac{m_{\text{heat sink}}\, C_{p,\text{heat sink}}\,(T_{\text{module}} - T_{\infty})}{t}, \quad (A.4b)$$

$$\Delta\dot{E}_{\text{PCM, stored}} = \frac{m_{\text{PCM}}\, C_{p,\text{PCM}}\,(T_{\text{module}} - T_{\infty})}{t} + \frac{\lambda\, m_{\text{PCM}}\, H_{\text{lat,PCM}}}{t}. \quad (A.4c)$$

$$\lambda = \begin{cases} 0, & T_{\text{module}} < T_{\text{s}} \\ \frac{T_{\text{module}} - T_{\text{s}}}{T_{\text{l}} - T_{\text{s}}}, & T_{\text{s}} \le T_{\text{module}} \le T_{\text{l}} \\ 1, & T_{\text{module}} > T_{\text{l}} \end{cases} \quad (A.5)$$

Notes: (1) In the equations above, the module's average temperature at the instant, T_{module}, was approximated as the average between the recorded temperatures at the top and base surfaces of the heat sink ($(T_{base}+T_{top})/2$). Note that the temperature recorded at the base surface of the heat sink, T_{base}, coincides with the electronics temperatures in this study, T. (2) In these equations, ambient temperature T_{∞} denotes the shroud temperature of the thermal vacuum chamber.

The net heat input to the sink's base surface, P_{module}, is first calculated from the energy balance as the sum of the increment energy stored in the module, $\Delta\dot{E}_{module}$, and the heat dissipated to surroundings via radiation, $q_{module,rad}$, (Eqs. (A.2), (A.3), (A.4a)). To reduce noise, the terms involved in the calculation of P_{module} were averaged over a moving time window from the terrestrial experimental works conducted in high-grade vacuum in the Wombat-XL TVAC, displayed in Fig. A.1.

Figs. A.2(a) and A.2(b) show the components of $\Delta\dot{E}_{module,stored}$ ($\Delta\dot{E}_{heatsink,stored}$ and $\Delta\dot{E}_{PCM,stored}$) and $q_{module,rad}$ for both thermal management modules. For the finned heat sink with no PCM, the incremental thermal energy absorbed by the heat sink material, $\Delta\dot{E}_{heatsink,stored}$, starts at its highest at the beginning of heating, and slowly decreases as the module's temperature rise rate slows down. The heat dissipated from the heat sink walls via radiation $q_{module,rad}$ increased as the heating progressed due to a higher temperature gradient between the heat sink and the environment. The ratio P_{module}/P_{heater} between the net heat flux delivered into the base of the sink and the electric heater input, begins near unity but gradually decreases. This behaviour indicates that the conduction losses through satellite structure slightly grow with time, attributed to an increased temperature gradient between the heat sink's base surface and ambient ($T_{base} - T_{\infty}$). For the IWP-TPMS PCM module, the adopted melting duration of PCM ranged from approximately 400 s, when T_{base} reached 53 °C, to around 950 s, when T_{top} reached 58 °C. As observed in Fig. A.2(b), within the PCM melting region, the thermal energy stored by the PCM, $\Delta\dot{E}_{PCM,stored}$, significantly contributed to an increase in the total energy stored by the module, $\Delta\dot{E}_{module,stored}$, and, therefore, an increased value of P_{module}/P_{heater}. During this time, it was also observed that the metallic heat sink's incremental energy absorption rate ($\Delta\dot{E}_{heatsink,stored}$) decreased compared to pre and post melting, due to the flattening of the temperatures during the PCM melting stage.

Representing the fraction of heater power that is lost through the satellite structure, the ratio P_{module}/P_{heater} is expected to be identical in both modules, since the structural configuration remains unchanged between them. When plotted against $T_{base} - T_{\infty}$, the results were approximated to a linear trend for both datasets (Fig. A.3) for comparison. The slight difference observed between the two trend lines may be attributed to imprecision in the PCM melting interval and variations in its instantaneous liquid fraction, which are difficult to be precisely captured in experiments. Since the two fitted trend lines were similar and should theoretically coincide, an equidistant line (and expression) between both modules' trend lines was created. The product of this equidistant expression for P_{module}/P_{heater} and the heater power P_{heater} from Eq. (1) comprises the applied heat flux boundary condition at the sink's base and is denoted in Eq. (2).

Appendix B. Heat sinks drawings

See Fig. B.4.

References

[1] Yunus A. Çengel, Heat and Mass Transfer: a Practical Approach, third ed., in: McGraw-Hill Series in Mechanical Engineering, McGraw-Hill, Boston, 2007.

[2] Z.M. Wan, G.Q. Guo, K.L. Su, Z.K. Tu, W. Liu, Experimental analysis of flow and heat transfer in a miniature porous heat sink for high heat flux application, Int. J. Heat Mass Transfer 55 (15–16) (2012) 4437–4441.

[3] Atul Sharma, V.V. Tyagi, C.R. Chen, D. Buddhi, Review on thermal energy storage with phase change materials and applications, Renew. Sustain. Energy Rev. 13 (2) (2009) 318–345.

[4] Raza Gulfam, Peng Zhang, Zhaonan Meng, Advanced thermal systems driven by paraffin-based phase change materials – A review, Appl. Energy 238 (2019) 582–611.

[5] Sol Z. Fixler, Satellite thermal control using phase-change materials, J. Spacecr. Rockets 3 (9) (1966) 1362–1368.

[6] Prabhu Bose, Valan Arasu Amirtham, A review on thermal conductivity enhancement of paraffinwax as latent heat energy storage material, Renew. Sustain. Energy Rev. 65 (2016) 81–100.

[7] Hassan Nazir, Mariah Batool, Francisco J. Bolivar Osorio, Marllory Isaza-Ruiz, Xinhai Xu, K. Vignarooban, Patrick Phelan, Inamuddin, Arunachala M. Kannan, Recent developments in phase change materials for energy storage applications: A review, Int. J. Heat Mass Transfer 129 (2019) 491–523.

[8] Raja Elarem, Talal Alqahtani, Sofiene Mellouli, Faouzi Askri, Abhilash Edacherian, Tirth Vineet, Irfan Anjum Badruddin, Jemni Abdelmajid, A comprehensive review of heat transfer intensification methods for latent heat storage units, Energy Storage 3 (1) (2021).

[9] Shengqi Zhang, Simone Mancin, Liang Pu, A review and prospective of fin design to improve heat transfer performance of latent thermal energy storage, J. Energy Storage 62 (2023) 106825.

[10] Krishnan Swaminathan Gopalan, Vinayak Eswaran, Numerical investigation of thermal performance of PCM based heat sink using structured porous media as thermal conductivity enhancers, Int. J. Therm. Sci. 104 (2016) 266–280.

[11] Yuandong Guo, Huning Yang, Guiping Lin, Haichuan Jin, Xiaobin Shen, Jiang He, Jianyin Miao, Thermal performance of a 3D printed lattice-structure heat sink packaging phase change material, Chin. J. Aeronaut. 34 (5) (2021) 373–385.

[12] Laryssa Sueza Raffa, Matt Ryall, Nick S. Bennett, Lee Clemon, Experimental investigation of the performance of a phase change material thermal management module under vacuum and atmospheric pressure conditions, Int. J. Heat Mass Transfer 236 (2025) 126384.

[13] Shen Du, Dong Li, Meng-Jie Li, Ya-Ling He, Numerical study on the effective thermal conductivity and thermal tortuosity of porous media with different morphologies, Sci. China Technol. Sci. 67 (6) (2024) 1685–1694.

[14] Xueliang Bai, Patrick Oppel, Iver H. Cairns, Xiaofeng Wu, Youngho Eun, Andrew G. Dempster, Ignatius Bramananditya Rivaldi, Nick S. Bennett, Roger Kermode, Laryssa S. Raffa, Mohammad Arqam, Matt Ryall, Anita Ho-Baillie, Laura Granados Caro, Shi Tang, Waratah seed-1: Australia's first commercial ride share satellite, in: SSC24-S4-04, 2024.

[15] EOS aluminium AlF357 material data sheet.

[16] Laryssa Sueza Raffa, Matt Ryall, Nick S. Bennett, Lee Clemon, Additively manufactured phase change material heat sinks for satellite thermal management, Appl. Therm. Eng. 286 (2026) 129325.

[17] David Gilmore, Spacecraft Thermal Control Handbook, Volume I: Fundamental Technologies, American Institute of Aeronautics and Astronautics, Inc., Washington, DC, 2002.

[18] Mohammad Arqam, Laryssa Sueza Raffa, Lee Clemon, Mohammad Saidul Islam, Matt Ryall, Nick S. Bennett, Numerical and experimental investigation of a phase change material radial fin heat sink for electronics cooling, J. Energy Storage 98 (2024) 113113.

[19] Sigma-aldrich product specification: Paraffin wax 327204.

[20] Laryssa Sueza Raffa, Matt Ryall, Iver H. Cairns, Nick S. Bennett, Lee Michael Clemon, Investigating the performance of a heat sink for satellite avionics thermal management: From ground-level testing to space-like conditions, Int. J. Heat Mass Transfer 248 (2025) 127139.

[21] CelesTrack, NORAD two line elements data from "active satellites", 2025, (Last Access 05 June 2025).

[22] S. Corpino, M. Caldera, F. Nichele, M. Masoero, N. Viola, Thermal design and analysis of a nanosatellite in low earth orbit, Acta Astronaut. 115 (2015) 247–261.

[23] Mohamed Katish, Stephen Allen, Adam Squires, Veronica Ferrandiz-Mas, Thermal stability of organic Phase Change Materials (PCMs) by accelerated thermal cycling technique, Thermochim. Acta 737 (2024) 179771.

[24] David S. Smith, Arnaud Alzina, Julie Bourret, Benoît Nait-Ali, Fabienne Pennec, Nicolas Tessier-Doyen, Kodai Otsu, Hideaki Matsubara, Pierre Elser, Urs T. Gonzenbach, Thermal conductivity of porous materials, J. Mater. Res. 28 (17) (2013) 2260–2272.

[25] Iñaki Garmendia, Haritz Vallejo, Miguel Seco, Eva Anglada, Design and fabrication of a phase change material heat storage device for the thermal control of electronics components of space applications, Aerospace 9 (3) (2022) 126.

[26] Wan-fan Wu, Na Liu, Wen-long Cheng, Yi Liu, Study on the effect of shape-stabilized phase change materials on spacecraft thermal control in extreme thermal environment, Energy Convers. Manage. 69 (2013) 174–180.

[27] Esam Alawadhi, Cristina Amon, PCM thermal control unit for portable electronic devices: Experimental and numerical studies, Components Packag. Technol. IEEE Trans. on 26 (2003) 116–125.

[28] Hong Ye, H. He, X. Ge, Bin Xu, Comparative numerical investigations on the melting process of form-stable phase change material using enthalpy formulation method and effective heat capacity formulation method, Taiyangneng Xuebao/Acta Energiae Solaris Sin. 25 (2004) 488–491.

[29] Namkyu Lee, Hyung Hee Cho, Thermal design of operating parameter for reliable AlSi7Mg selective laser melting, J. Mater. Res. Technol. 30 (2024) 4405–4411.

[30] Soo-Jin Kang, Hyun-Ung Oh, On-Orbit Thermal Design and Validation of 1 U Standardized CubeSat of STEP Cube Lab, Int. J. Aerosp. Eng. 2016 (2016) 1–17, http://www.hindawi.com/journals/ijae/2016/4213189/.

[31] Laryssa Sueza Raffa, Matt Ryall, Lee Michael Clemon, Nick S. Bennett, In-orbit thermal resilience: Demonstration of a triply periodic minimal surface heat sink with phase change material aboard the matilda payload on waratah seed-1 CubeSat, Submitt. Appl. Therm. Eng. J. (2026).

[32] Sydney Taylor, Neal Boman, Jeremy Chao, Liping Wang, Cryothermal vacuum measurement of thermochromic variable-emittance coatings with heating/cooling hysteresis for spacecraft thermal management, Appl. Therm. Eng. 199 (2021) 117561.